



HAL
open science

Sequential double photodetachment of He^- in elliptically polarized laser fields

Matthieu Génévriez, Kevin M. Dunseath, Mariko Dunseath-Terao, Xavier Urbain

► To cite this version:

Matthieu Génévriez, Kevin M. Dunseath, Mariko Dunseath-Terao, Xavier Urbain. Sequential double photodetachment of He^- in elliptically polarized laser fields. *Physical Review A: Atomic, molecular, and optical physics* [1990-2015], 2018, 97 (2), pp.023412. 10.1103/PhysRevA.97.023412. hal-01708561

HAL Id: hal-01708561

<https://hal.science/hal-01708561>

Submitted on 3 Jul 2018

HAL is a multi-disciplinary open access archive for the deposit and dissemination of scientific research documents, whether they are published or not. The documents may come from teaching and research institutions in France or abroad, or from public or private research centers.

L'archive ouverte pluridisciplinaire **HAL**, est destinée au dépôt et à la diffusion de documents scientifiques de niveau recherche, publiés ou non, émanant des établissements d'enseignement et de recherche français ou étrangers, des laboratoires publics ou privés.

Sequential double photodetachment of He^- in elliptically polarized laser fields

Matthieu Génévriez,^{1,*} Kevin M. Dunseath,² Mariko Terao-Dunseath,² and Xavier Urbain^{1,†}

¹*Institute of Condensed Matter and Nanosciences,*

Université catholique de Louvain, Louvain-la-Neuve B-1348, Belgium

²*Univ Rennes, CNRS, IPR (Institut de Physique de Rennes) - UMR 6251, F-35000 Rennes, France*

Four-photon double detachment of the helium negative ion is investigated experimentally and theoretically for photon energies where the transient helium atom is in the $1s2s\ ^3S$ or $1s2p\ ^3P^o$ states, which subsequently ionize by absorption of 3 photons. Ionization is enhanced by intermediate resonances, giving rise to series of peaks in the He^+ spectrum, which we study in detail. The He^+ yield is measured in the wavelength ranges from 530 nm to 560 nm and from 685 nm to 730 nm and for various polarizations of the laser light. Double detachment is treated theoretically as a sequential process, within the framework of R -matrix theory for the first step and effective Hamiltonian theory for the second step. Experimental conditions are accurately modeled, and the measured and simulated yields are in good qualitative and, in some cases, quantitative agreement. Resonances in the double detachment spectra can be attributed to well defined Rydberg states of the transient atom. The double detachment yield exhibits a strong dependence on the laser polarization which can be related to the magnetic quantum number of the intermediate atomic state. We also investigate the possibility of non-sequential double detachment with a two-color experiment but observe no evidence for it.

I. INTRODUCTION

Double photodetachment, the process in which a negative ion absorbs one or several photons and ejects two electrons, has been much less studied than double photoionization, its counterpart for atoms and positive ions [1]. While the important structural differences between anions and atoms are expected to alter the dynamics of double electron ejection, experimental investigation however has been hampered by the difficulty of producing anions in sufficiently high density.

Early work on double photodetachment involved moderately intense fields ($\sim 10^{10}\ \text{W}\cdot\text{cm}^{-2}$) and aimed at either studying excess photon detachment, *i.e.* the absorption by the system of more photons than is energetically required, or at performing spectroscopy of autoionizing states embedded in the continuum [2, 3]. The detection of positive ions following photodetachment is also at the basis of resonant ionization spectroscopy, although in this case the atom is optically excited to a Rydberg state and ionized by a static electric field [4]. In these studies, the production of positive ions is a means to study single photodetachment of the negative ion, and the ionization dynamics of the second electron from the neutral atom are not considered in detail. More recently, a number of studies have been devoted to double detachment in an intense field ($\geq 10^{13}\ \text{W}\cdot\text{cm}^{-2}$), where the absence of a long-range Coulomb potential and the lower binding energy compared to atoms are expected to significantly modify the dynamics of non-sequential processes [5–10].

The work reported here concerns double detachment of the $1s2s2p\ ^4P^o$ metastable state of He^- in moderately

strong laser fields, with intensities comparable to those of earlier work [2, 3], where multiphoton processes dominate. While no other experimental or theoretical data is available for this anion, the choice of such a few-electron system allows the physics to be studied in detail both experimentally and theoretically. For moderate intensities, the process can be treated as sequential, *i.e.* as single photodetachment of the anion followed by ionization of the neutral atom. The first step, shown schematically on the left-hand side of Fig. 1, involves the one-photon detachment of He^- ; this has already been studied both experimentally and theoretically, with good overall agreement [11–13]. Detachment in the wavelength ranges from 530 nm to 560 nm and from 685 nm to 730 nm leaves helium in the $1s2s\ ^3S$ and $1s2p\ ^3P^o$ states, which can subsequently ionize by absorption of three photons, as shown on the right-hand side of Fig. 1.

It has already been shown that multiphoton ionization of excited helium atoms is greatly enhanced by resonances with higher-lying states [14–17], a process known as Resonance Enhanced MultiPhoton Ionization (REMPI). In a previous paper [18], hereafter referred to as paper P1, we investigated three-photon ionization of $\text{He}(1s2p\ ^3P^o)$, observing two-photon resonances with Rydberg states as well as an extra resonant pathway via the low-lying $1s3s\ ^3S$ state which further complicates the ionization dynamics. Using the same experimental setup and effective Hamiltonian approach, we here extend the study reported in P1 over a wider range of photon energies and investigate the effect of different laser polarizations. The first, photodetachment step is also treated in more detail.

We have shown in paper P1 that the magnetic quantum number M influences the double detachment dynamics since for $M = 0$, extra ionization pathways are allowed. The influence of M on double detachment in strong laser fields has also been discussed within the

* Present address: Laboratory of Physical Chemistry, ETH Zurich, CH-8093 Zurich, Switzerland

† xavier.urbain@uclouvain.be

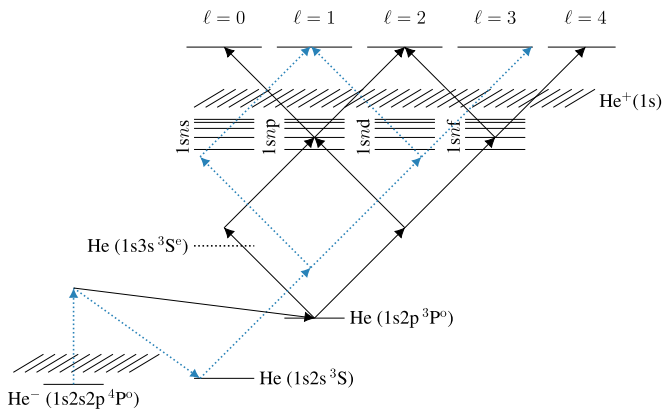


FIG. 1. Schematic energy level diagram of He⁻ and He⁺. The dotted arrows show the pathway responsible for double detachment of He⁻ via the 1s2s intermediate state and through (2+1) REMPI (Resonance Enhanced MultiPhoton Ionization) of the atom. The solid arrows show the pathway via the 1s2p state and through (1+1+1) and (2+1) REMPI of the atom.

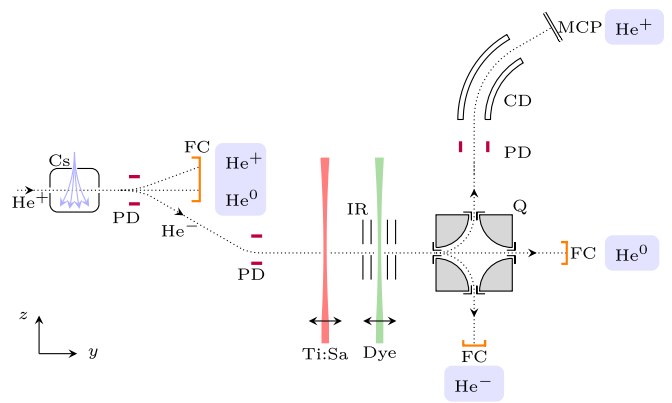


FIG. 2. Experimental setup. Cs: cesium vapor cell; PD: planar deflector; FC: Faraday cup; CD: cylindrical deflector; IR: biased interaction region; Q: quadrupole deflector; MCP: multichannel plates; Ti:Sa: Ti:Sapphire laser beam; Dye: dye laser beam. Double arrows indicate convergent lenses. The laser beams propagate along the z direction and their polarizations, when linear, are along the y axis.

74 framework of Ammosov-Delone-Krainov or Keldysh-like
75 models [8, 9], and was shown to be of some importance in
76 the saturation of the second, ionization step. This influ-
77 ence will also be investigated below, in particular how it
78 depends on the wavelength and polarization of the laser
79 light.

80 The paper is organized as follows: the experimental
81 setup is briefly described in Section II; the R -matrix cal-
82 culation for the photodetachment of He⁻ together with
83 the effective Hamiltonian approach used to treat ioniza-
84 tion of helium are presented in Section III. Section IV
85 presents and discusses the experimental and theoretical
86 results.

87 II. EXPERIMENTAL SETUP

88 The experimental setup, presented in Fig. 2, is es-
89 sentially the same as in paper P1. We therefore give
90 only a brief summary of its main features but describe in
91 more detail the few modifications required for the present
92 study.

93 A beam of He⁺ ions is first extracted from a duoplas-
94 matron source, accelerated to 4 keV and mass selected by
95 a permanent magnet. Negative helium ions He⁻(1s2s2p
96 ⁴P^o) are produced by double charge transfer with cesium
97 atoms in a vapor cell, with an efficiency of about
98 1%. Double electrostatic deflection subsequently clears
99 the He⁻ beam of its positive (He⁺) and neutral (He⁰)
100 components before it enters the region of interaction with
101 the laser beam, pumped to high vacuum ($\sim 10^{-8}$ mbar).
102 Although He⁻(1s2s2p⁴P^o) is metastable, the lifetimes
103 of its $J = 1/2, 3/2$ and $5/2$ fine structure components,
104 7.8 μ s, 12.3 μ s and 359 μ s respectively [19], are suffi-
105 ciently long to perform the experiment using conventional
106 beam transport techniques. Contamination of the beam

107 by ground state helium atoms due to spontaneous de-
108 tachment is very weak, of the order of one percent.

109 The ion beam is illuminated by nanosecond laser pulses
110 from a tunable dye laser pumped by the second or third
111 harmonics of a Q-switched Nd:YAG laser. Coumarin 500
112 and Pyridine 1-2 dyes were used to cover wavelength
113 ranges from 530 nm to 560 nm and from 685 nm to
114 730 nm respectively. At the laser output, the pulse en-
115 ergy is attenuated to the required value by the combina-
116 tion of a $\lambda/2$ plate mounted on a high accuracy rotation
117 stage and a polarizing beam splitter. Laser light is then
118 focused onto the ion beam inside the vacuum chamber
119 by an $f = 40$ cm lens and collected, as it exits the cham-
120 ber, by a pulse energy meter. The attenuation system
121 is servo-controlled in order to maintain a constant pulse
122 energy throughout the dye gain curve. The size of the
123 waist at focus is about 54 μ m, resulting in a peak inten-
124 sity of 2.9×10^{10} W/cm² for 6 mJ pulses. A $\lambda/4$ -plate
125 is placed between the attenuator and the lens to change
126 the polarization of the laser beam from linear to circular
127 or elliptic. To avoid spurious depolarisation, no mirrors
128 are used beyond the $\lambda/4$ -plate.

129 Ions cross the laser spot (twice the waist) in about
130 250 ps, an interval much shorter than the duration of the
131 laser pulse itself (~ 5 ns FWHM). During their transit,
132 some ions undergo photodetachment and the resulting
133 neutral atoms can further be ionized by absorbing 3 more
134 photons. Beyond the interaction region, the He⁺ ions are
135 analyzed in energy by a quadrupole deflector combined
136 with a 60° cylindrical deflector and an analyzing slit, and
137 detected by micro-channel plates (MCP). The anions are
138 collected on the other side of the quadrupole by a Far-
139 aday cup. In order to collect only those He⁺ ions produced
140 by photodetachment and ionization within the same dye
141 laser pulse, a bias of 100 V is applied to the interaction
142 region with the dye laser. He⁺ ions produced by double

143 detachment of He^- in this region gain an energy of 200
 144 eV while those produced by ionization of incoming He
 145 atoms gain only 100 eV. He^+ ions produced by collisions
 146 with the residual gas outside the interaction region gain
 147 no energy. The subsequent energy analysis performed by
 148 the quadrupolar and cylindrical deflectors readily sepa-
 149 rates the various contributions. Moreover, the detection
 150 of laser-induced He^+ ions is performed only in a narrow
 151 time-window centered around their time-of-flight from
 152 the interaction region. A second, time-shifted window
 153 is used to measure the background signal. The selection
 154 in energy and time-of-flight ensures quasi background-
 155 free measurements, with less than 3 background counts
 156 per hundred laser shots.

157 In order to assess the sequential nature of the dou-
 158 ble detachment process, we have performed a two-color
 159 experiment where helium atoms are first prepared in the
 160 $1s2p$ state outside the interaction region by photodetach-
 161 ment by a CW Ti:Sapphire laser and ionized downstream
 162 by pulses from the dye laser. By operating the tun-
 163 able CW laser at a wavelength of 1005 nm, more than
 164 99% of photodetachment occurred into $\text{He}(1s2p\ ^3P^o)$ as
 165 the cross section of this process reaches a maximum of
 166 $3.6 \times 10^{-19} \text{ m}^2$ due to a resonance with the $\text{He}^-(1s2p^2$
 167 $^4P^e)$ autodetaching state [11, 12]. During transit between
 168 the two laser foci, separated by less than 1 cm, 20% of the
 169 $\text{He}(1s2p\ ^3P^o)$ states decay spontaneously into $\text{He}(1s2s$
 170 $^3S)$. By selecting downstream those ions that gained a
 171 kinetic energy of 100 eV, we could detect He^+ ions pro-
 172 duced by sequential, two-color detachment and ionization
 173 only.

174 III. THEORY

175 A. Single photodetachment of He^-

176 One-photon detachment of He^- has been studied in
 177 some detail over the past few decades, with particular
 178 emphasis on resonances due to doubly excited states em-
 179 bedded in the continuum (see the review article [1] and
 180 references therein). In the wavelength ranges spanned by

181 the present study (530-560 nm and 685-730 nm), no such
 182 resonances are accessible and the cross section exhibits no
 183 sharp variation. Overall, there is relatively good agree-
 184 ment between the various theoretical and experimental
 185 results in this region [11–13, 20–25]. Previous studies
 186 however only dealt with *linear* polarization, whilst the
 187 present goal is to study double detachment in an el-
 188 liptically polarized field. Moreover, while partial cross
 189 sections for photodetachment into the $\text{He}(1s2s\ ^3S)$ and
 190 $\text{He}(1s2p\ ^3P^o)$ states have been considered by some au-
 191 thors, no data exist for partial cross sections to the vari-
 192 ous magnetic sublevels of a final state, *e.g.*, $\text{He}(1s2p\ ^3P^o)$
 193 with magnetic quantum numbers $M_f = 0, \pm 1$. Such par-
 194 tial cross sections are not anecdotal since, for example,
 195 the dynamics of resonance-enhanced multiphoton ioniza-
 196 tion of $\text{He}(1s2p\ ^3P^o)$ strongly depends on M_f (see paper
 197 P1). We have thus derived a formula for partial cross
 198 sections to the magnetic sublevels of a given state and
 199 calculated their values in the desired wavelength range
 200 based on reduced dipole matrix elements obtained from
 201 an R -matrix calculation.

202 In what follows, we assume L - S coupling and consider
 203 only dipole-allowed transitions. Since the initial state
 204 ($1s2s2p\ ^4P^o$) has a total spin $S_i = 3/2$, the dipole selec-
 205 tion rules impose that the residual atom is left in a triplet
 206 state. For ease of notation, we therefore do not explicitly
 207 specify the spin quantum numbers in what follows.

208 We consider an initial state of the unpolarized anion,
 209 denoted by $|\alpha_i L_i M_i\rangle$, where L_i is the total orbital angu-
 210 lar momentum of the state i , M_i its magnetic quantum
 211 number and where α_i represents all other quantum num-
 212 bers required to specify the state. The residual atom is
 213 left in a state $|\alpha_f L_f M_f\rangle$ of total orbital angular momen-
 214 tum L_f and magnetic quantum number M_f . The ejected
 215 electron is described by continuum orbitals $|\epsilon_f \ell_f m_f\rangle$ of
 216 energy ϵ_f , orbital angular momentum ℓ_f and magnetic
 217 quantum number m_f . The final continuum state of total
 218 angular momentum L and magnetic quantum number
 219 M , denoted by $|\alpha_f L_f \ell_f L M\rangle$, is obtained by coupling to-
 220 gether the residual atom wave function and continuum
 221 orbitals. The length form of the partial cross section for
 222 photodetachment to a particular magnetic sublevel, aver-
 223 aged over the initial states and summed over the possible
 224 spin projections of the final states is given by

$$\sigma_{\alpha_f L_f M_f}(\hat{\epsilon}) = \frac{4\pi^2 \alpha a_0^2 \omega}{2L_i + 1} \sum_{M_i} \sum_{L, L'} \sqrt{(2L + 1)(2L' + 1)} \sum_{\ell_f, m_f} \begin{pmatrix} L_f & \ell_f & L \\ M_f & m_f & -M \end{pmatrix} \begin{pmatrix} L_f & \ell_f & L' \\ M_f & m_f & -M \end{pmatrix} \\ \times \langle \alpha_f L_f \ell_f L' M | D(\hat{\epsilon}) | \alpha_i L_i M_i \rangle^* \langle \alpha_f L_f \ell_f L M | D(\hat{\epsilon}) | \alpha_i L_i M_i \rangle, \quad (1)$$

which is derived from the general expression of the dipole
 matrix elements given by Burke [26], and where α is the
 fine-structure constant, a_0 is the Bohr radius, ω is the
 photon angular frequency and $D(\hat{\epsilon})$ is the dipole length

operator for a given polarization vector $\hat{\epsilon}$. In the “natu-
 ral” reference frame of Tumaikin and Yudin [27, 28], this

is expressed as

$$\hat{\epsilon} = \mathbf{e}_0 \sqrt{\cos 2\varepsilon} - \mathbf{e}_{\pm 1} \sqrt{2} \sin \varepsilon \quad (2)$$

where $\mathbf{e}_{0,\pm 1}$ are spherical unit vectors [29] and the ellipticity angle ε can take the values $-\pi/4 \leq \varepsilon \leq \pi/4$. On the right-hand side, the helicity of the vector $\mathbf{e}_{\pm 1}$ corresponds to the sign of ε . The polarization is linear when $\varepsilon = 0$, left circular when $\varepsilon = \pi/4$ and right circular when $\varepsilon = -\pi/4$. The choice of reference frame is arbitrary, and a commonly used convention is to choose the quantization axis z along the electric field in the case of linear polarization, and along the direction of light propagation in the case of circular polarization. The natural frame possesses the advantage of bridging these two conventions by performing a continuous rotation of the reference frame

as the ellipticity angle evolves from 0 to $\pm\pi/4$. The orientation of the reference frame in the laboratory frame thus depends on the ellipticity angle, and it is identical to standard conventions in the limiting cases of linear and circular polarization. Any other frame would yield identical results for the partial photodetachment cross sections, keeping in mind that the M values are projections of the angular momentum along the quantization axis, and an appropriate rotation must therefore be performed in order to make meaningful comparisons.

With the definition (2) for the polarization vector, the dipole matrix elements appearing in (1) can be obtained from the reduced matrix elements $\langle \alpha_f L_f \ell_f L_f | \mathbf{D} | \alpha_i L_i \rangle$ using the Wigner-Eckart theorem [29]:

$$\langle \alpha_f L_f \ell_f L_f | D(\hat{\epsilon}) | \alpha_i L_i M_i \rangle = (-1)^{-L-M} \left[\begin{pmatrix} L & 1 & L_i \\ -M & 0 & M_i \end{pmatrix} \sqrt{\cos 2\varepsilon} - \begin{pmatrix} L & 1 & L_i \\ -M & \pm 1 & M_i \end{pmatrix} \sqrt{2} \sin \varepsilon \right] \langle \alpha_f L_f \ell_f L_f | \mathbf{D} | \alpha_i L_i \rangle, \quad (3)$$

where \mathbf{D} is the tensor operator corresponding to $D(\hat{\epsilon})$. Note that the reduced matrix element does *not* depend on the polarization.

The cumulated photodetachment probability to a particular final state $|\alpha_f L_f M_f\rangle$ is readily obtained from the partial cross sections by solving the rate equation $dN(t)/dt = -\sigma\phi(t)N(t)$ with appropriate boundary conditions,

$$P_{L_f M_f}(t) = \frac{\sigma_{\alpha_f L_f M_f}}{\sigma} \times \left[1 - e^{-\int_{-\infty}^t dT \sigma \phi(T)} \right], \quad (4)$$

where $\phi(T)$ is the instantaneous photon flux and the total cross section σ is obtained by summing the partial cross sections over all quantum numbers. Note that the intensity, or photon flux, required for double detachment is very high and therefore, in the region where it occurs, the exponential term on the right hand side of the above equation is essentially zero, *i.e.* photodetachment is saturated.

In order to compute the partial cross sections (1, 3) and hence the cumulated photodetachment probability, we require the reduced dipole matrix elements $\langle \alpha_f L_f \ell_f L_f | \mathbf{D} | \alpha_i L_i \rangle$, which are independent of the polarization. In the work reported here, these were obtained from a standard R -matrix calculation including the five lowest triplet states of helium (1s2s 3S , 1s2p $^3P^o$, 1s3s 3S , 1s3p $^3P^o$, 1s3d 3D), using the UK APAP (Atomic Processes for Astrophysical Plasmas) suite of computer codes [30]. Details are given in the appendix.

B. Three-photon ionization of He

After the first electron is ejected from He⁻, and the neutral atom moves forward through the laser pulse, the intensity rises. If the photon energy is appropriately chosen, the intensity may become sufficiently high to favor the (1+1+1) or (2+1) REMPI of the atom. In P1, we have shown that Effective Hamiltonian (EH) theory can provide an accurate description of the phenomenon and hence can be used to model the experiment in detail. EH theory has been described in some length elsewhere [31–33], so we shall only briefly summarize it here, concentrating on the details relevant to the present study.

In EH theory, Hilbert space is partitioned into two different subspaces: the model space \mathcal{P} contains the quasis resonant bound states, and its orthogonal complement \mathcal{Q} spans the rest of Hilbert space. The effective Hamiltonian is built from the exact Hamiltonian of the \mathcal{P} -space, while the \mathcal{Q} -space is included through additional, perturbative matrix elements coupling model-space states. In this respect, EH theory can be considered as a semiperturbative treatment of multiphoton ionization. Choice of the \mathcal{P} -space is critical since it must be small enough so that the effective Hamiltonian matrix is kept small and calculations are relatively simple, and yet contain all states essential for the REMPI dynamics.

The effective Hamiltonian H_{eff} satisfies the following eigenvalue equation

$$H_{\text{eff}} |\psi_p\rangle = E |\psi_p\rangle, \quad (5)$$

where $|\psi_p\rangle$ is the model space wave function. Each eigen-

value can be written as $E = E_0 + \Delta - i\frac{\Gamma}{2}$, the real part being the Stark-shifted energy of the field-dressed atomic state and Γ its total ionization width. The effective Hamiltonian valid up to the second order of perturbation theory is

$$H_{\text{eff}} = PH_0P + PVP + P\left(S + \Omega - i\frac{\Gamma}{2}\right)P \quad (6)$$

where V is the exact atom-field interaction operator and H_0 is the exact “free” Hamiltonian, containing the field-free atomic and light-field Hamiltonians. P is the Feshbach projection operator, projecting the wave function onto \mathcal{P} -space states: $\sum_{i \in \mathcal{P}} |i\rangle \langle i|$. The operator S is a two-photon transition operator connecting the \mathcal{P} -space states *via* nonresonant bound states and the operators Ω and Γ represent two-photon couplings between model-space states through the ionization continua (see P1 for the detailed expression of these operators).

The eigenvalues of H_0 for bound states are $E_i = \mathcal{E}_i - N\omega$, where \mathcal{E}_i is the field-free energy of the bound state and N is the number of photons absorbed. Field-free energies for low-lying bound states ($n \leq 3$) are taken from the NIST atomic database [34]. The energies of Rydberg states are computed from their principal quantum number n and quantum defect $\delta_{n\ell}$. The latter is calculated using Ritz’s expansion with coefficients given by Drake [35]. By convention, $N = 0$ for either of the 1s2s

or 1s2p initial states, $N = 1$ for the 1s3s and 1s3d states and $N = 2$ for the Rydberg states. The eigenvalues of the continuum states of H_0 are, similarly, $e = \epsilon_f - 3\omega$, where ϵ_f is the photoelectron energy.

The one- and two-photon matrix elements (V_{ij} , S_{ij} , Ω_{ij} and Γ_{ij}) coupling states of the model space are expressed within the dipole and rotating-wave approximations [36], justified by the moderate laser intensities and the explicit treatment of only quasis resonant bound states. Their calculation for all polarization states $\hat{\epsilon}$ is prohibitive, but can be greatly simplified, as for the photodetachment of He^- , by virtue of the Wigner-Eckart theorem. Reduced matrix elements, independent of $\hat{\epsilon}$, are calculated only once using: (i) two-electron DVR basis functions for couplings between low-lying states; (ii) Quantum Defect wave functions for couplings amongst Rydberg states and between Rydberg and continuum states (see paper P1). Dipole matrix elements for any, arbitrary $\hat{\epsilon}$ are then readily calculated using Eq. (3) and the effective Hamiltonian matrix is then constructed using these elements.

We have built two effective Hamiltonians to describe the REMPI of the 1s2s and 1s2p initial states respectively. For the 1s2s state, ionization proceeds *via* a two-photon resonance with the Rydberg 1sns and 1snd states. The model space includes the 1s2s, 1sns and 1snd states with n in the range from 4 to 27, and the wave function is expressed as

$$|\psi_p(t)\rangle = c_{2s0}(t) |2s0\rangle + \sum_{n=4}^{27} \left[c_{ns0}(t) |ns0\rangle + \sum_M c_{ndM}(t) |ndM\rangle \right]. \quad (7)$$

The 1s orbital has been omitted in the $|n\ell M\rangle$ basis vectors for brevity. The total orbital angular momentum L has also been omitted and is equal to that of the outer electron ($L = \ell$). The summation over the total magnetic quantum number M runs from $-\ell$ to $+\ell$ for each basis vector. For the 1s2p state, ionization proceeds through the (1+1+1) and (2+1) REMPI schemes shown in Fig. 1. The model space is thus spanned by one of the magnetic sublevels of the 1s2p state, defined by its magnetic quantum number M_f , and the 1s3s, 1s3d, 1snp and 1snf states. The wave function is given by

$$|\psi_p(t)\rangle = c_{2pM_f}(t) |2pM_f\rangle + c_{3s0}(t) |3s0\rangle + \sum_M \left\{ c_{3dM}(t) |3dM\rangle + \sum_{n=6}^{45} [c_{npM}(t) |npM\rangle + c_{nfM}(t) |nfM\rangle] \right\}. \quad (8)$$

For both initial states, the \mathcal{Q} -space is truncated to a finite size and includes only the bound and continuum states involved in two-photon couplings between \mathcal{P} -space states. It comprises bound states up to $n = 70$ and continuum states up to energies where bound-free couplings are negligible. For linear polarization, selection rules ($\Delta M = 0$) permit only those states with the same magnetic quantum number as the initial state to be populated. This in turn keeps the size of the effective Hamiltonian small, *e.g.*, 83×83 for the 1s2p initial state. In the general case of elliptic polarization, looser selection

rules ($\Delta M = 0, \pm 1$) yield a significantly larger effective Hamiltonian, with a size up to 409×409 for the 1s2p state.

Once the effective Hamiltonian is constructed, it is used to propagate the wave function along the atom’s trajectory through the laser pulse. This is done by solving the time-dependent Schrödinger equation [37], whose formal solution may be written as

$$|\psi_p(t + \Delta t)\rangle = e^{-iH_{\text{eff}}(t)\Delta t} |\psi_p(t)\rangle. \quad (9)$$

382 The wave function is iteratively propagated by comput-
 383 ing numerically the matrix exponential $e^{-iH\Delta t}$ with the
 384 EXPOKIT computer package [38]. The time dependence
 385 of the effective Hamiltonian arises from the dependence
 386 of the couplings between model-space states on the in-
 387 tensity of the laser field, itself evolving in time as the
 388 atom travels through the laser focus. The wave func-
 389 tion is propagated up to about $t = 4 \times 10^7$ a.u. in steps
 390 of $\Delta t \simeq 10^4$ a.u. The initial condition for propagation
 391 starting from the He(1s2s 3S) state is

$$|c_{2s0}(0)|^2 = P_{2s0}(t \rightarrow \infty), \quad (10)$$

392 where $P_{2s,0}$ is the detachment probability, given by
 393 Eq. (4). All other coefficients are zero. Similarly, the
 394 initial condition for the He(1s2p $^3P^o$) state is given by

$$|c_{2pM_f}(0)|^2 = P_{2pM_f}(t \rightarrow \infty), \quad (11)$$

395 and all other coefficients are zero. Such initial conditions
 396 imply that the photodetachment and ionization processes
 397 are sequential, and that the former occurs well before
 398 the latter, *i.e.* at much lower intensities. Due to the
 399 non-hermicity of the effective Hamiltonian, the norm of
 400 the wave function at the end of the propagation has de-
 401 creased by an amount p . This quantity corresponds to
 402 the probability of ejecting 2 electrons from the He $^-$ ion
 403 *via* either the He(1s2s 3S) state or one of the magnetic
 404 sublevels of the He(1s2p $^3P^o$) state. The total ejection
 405 probability p_{tot} is the sum over all channels. Note that
 406 for each photon energy, p_{tot} is computed for a range of
 407 peak intensities and appropriate averaging over the ion
 408 beam section and integration over the pulse duration is
 409 subsequently performed in order to simulate experimen-
 410 tal conditions (see paper P1). Simulated results are also
 411 multiplied by 0.56 to account for the MCP detection ef-
 412 ficiency.

413 IV. RESULTS AND DISCUSSION

414 A. Single photodetachment

415 We have studied the one-photon, single detachment of
 416 He $^-$ under elliptical polarization and in the wavelength
 417 range from 685 nm to 730 nm (1.698 eV to 1.810 eV).
 418 Branching ratios to He(1s2s 3S) and He(1s2p $^3P^o$, $M_f =$
 419 $0, \pm 1$) final states were calculated using Eq. (1) with
 420 reduced dipole matrix elements obtained from the R -
 421 matrix calculation described in the appendix. This
 422 calculation yielded an electron affinity of 75.5 meV,
 423 which compares favorably with the experimental value
 424 of 77.516 meV [39]. The total and partial cross sections
 425 are in good agreement with those of an earlier R -matrix
 426 calculation [11].

427 The branching ratios are in fact only weakly depen-
 428 dent on the wavelength. A representative set is shown

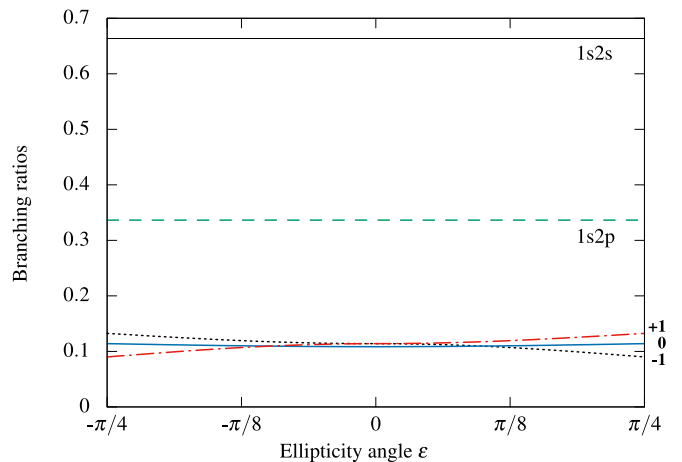


FIG. 3. Branching ratios $R_{2s,2p}$ for the photodetachment of He $^-$ into the He(1s2s 3S) and He(1s2p $^3P^o$) states at $\lambda = 690$ nm. Full thin line: 1s2s state, dashed line: 1s2p state. Branching ratios to the various magnetic sublevels of the 1s2p state are also shown, and corresponding M_f values are labeled on the right hand-side of the graph. Dotted line: $M_f = -1$, full thick line: $M_f = 0$, dash-dotted line: $M_f = +1$.

429 in Fig. 3, for different light polarizations at $\lambda = 690$ nm
 430 (1.797 eV). The population of the 1s2s state ($R_{2s} = 0.66$)
 431 is nearly twice that of the 1s2p state ($R_{2p} = 0.34$), and
 432 this sharing is independent of the ellipticity. The 1s2p
 433 state is slightly less populated at shorter wavelengths
 434 ($R_{2p} = 0.33$ for $\lambda = 685$ nm) and slightly more populated
 435 at longer wavelengths ($R_{2p} = 0.39$ for $\lambda = 730$ nm).

436 The branching ratio to the 1s2s state with a single,
 437 isotropic sublevel $M_f = 0$ does not depend on the el-
 438 lipticity. The 1s2p state has three magnetic sublevels
 439 with $M_f = 0, \pm 1$. The branching ratio for $M_f = 1$ and
 440 $M_f = -1$ respectively increases and decreases slightly as
 441 the ellipticity angle goes from 0 to $\pi/4$. The branching
 442 ratio for $M_f = 0$ is essentially independent of ellipticity,
 443 with only a slight (5%) increase between linear and circ-
 444 ular polarization. For linear polarization ($\varepsilon = 0$), the three
 445 sublevels are almost equally populated, with 34% in each
 446 of the $M_f = 1$ and -1 states and 32% in the $M_f = 0$
 447 state. For left circular polarization σ^+ ($\varepsilon = \pi/4$), the
 448 $M_f = 1$ state is preferentially populated with 39% of the
 449 total 1s2p population, compared to 34% in $M_f = 0$ and
 450 27% in $M_f = -1$. This may be expected since the dipole
 451 transition selection rule is $\Delta M = +1$. For right circ-
 452 ular polarization σ^- ($\varepsilon = -\pi/4$), the opposite behavior is
 453 observed with the $M_f = -1$ state being more populated.

454 The branching ratios to the various magnetic sublevels
 455 of the 1s2p state depend on the choice of the reference
 456 frame, since M_f values represent the projection of the
 457 orbital angular momentum onto the quantization axis z .
 458 In the natural reference frame, the polarization vector
 459 given by Eq. (2) rotates in the laboratory frame with
 460 the ellipticity angle, so that magnetic quantum numbers
 461 for different polarizations correspond to projections onto
 462 quantization axes with different orientations. Such de-

pendence however does not affect the final conclusions since all calculations to determine measurable quantities are performed within the same frame, and the final results are summed over all M_f values, *i.e.* all orientations, before being compared to experiment. As noted in the previous section, for linear ($\varepsilon = 0$) and circular ($\varepsilon = \pm\pi/4$) polarizations, the natural frame coincides with the standard choice of reference frame and comparisons with other data are straightforward. Moreover, calculations within other reference frames would yield results equivalent to the present ones and which can be compared to one another after appropriate rotation by means of Wigner D matrices [29].

We note that in paper P1, a population distribution of (0.25, 0.5, 0.25) was assumed for the (-1, 0, 1) magnetic sublevels of the $1s2p$ state for linear polarization, as it provided the best fit to some of the experimental results. The present calculation proves this assumption incorrect and, while it does not modify the conclusions drawn in P1, it changes to some extent the relative height of the $1snp$ and $1snf$ peaks in the simulated He^+ ion spectra.

The behavior of the branching ratios for magnetic sublevels is established here for photodetachment of He^- , but the trends observed most certainly hold for other anions. The magnitude of the photodetachment cross section depends on the reduced dipole matrix elements, but their dependence on magnetic number M_f and polarization $\hat{\varepsilon}$ derives from angular momentum algebra. Relatively small variations between different anions or final states are expected to arise since matrix elements and geometrical factors are entangled in the various summations of Eq. (1).

B. Double photodetachment

1. Transient $\text{He}(1s2s\ ^3S)$ state

We first consider double detachment in the photon energy range between 2.22 eV and 2.34 eV, corresponding to the wavelength region from 530 nm to 560 nm covered by the laser when supplied with Coumarin 500 dye. Inspection of the helium triplet spectrum indicates that the three-photon ionization of $\text{He}(1s2s\ ^3S)$ is strongly enhanced by two-photon resonances with Rydberg $1sns$ and $1snd$ states, as shown in Fig. 1, while the two-photon ionization of $\text{He}(1s2p\ ^3P^o)$ is non-resonant. One may thus expect double detachment to proceed preferentially through the $1s2s$ intermediate state, even though the number of photons required is higher than for the $1s2p$ state. This hypothesis is supported by the experimental spectrum for linear polarization, shown in Fig. 4(a). The spectrum represents the number of He^+ ions, created from an incoming He^- beam of 1 nA by a 6 mJ laser pulse, as a function of the photon energy. The two series of peaks correspond to two-photon excitation from $1s2s$ to respectively $1sns$ and $1snd$ states with $n = 7$ to $n = 12$, which are subsequently ionized by another

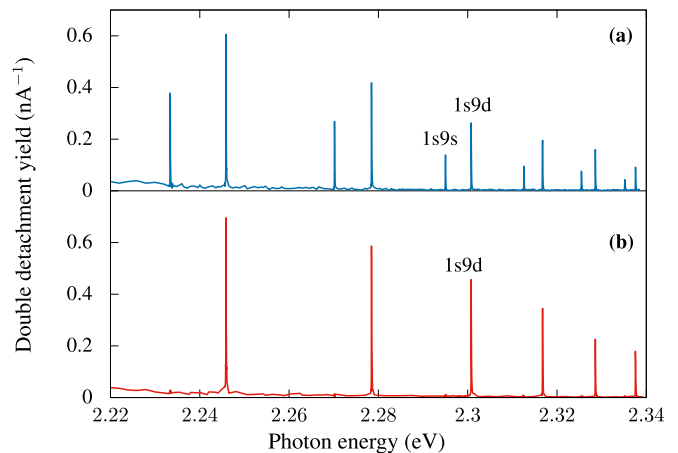


FIG. 4. Experimental double detachment spectrum as a function of the photon energy. Top graph (a): linear polarization. Bottom graph (b): left circular polarization. Data shown is the number of He^+ ions produced by a 6 mJ laser pulse and for a He^- beam of 1 nA .

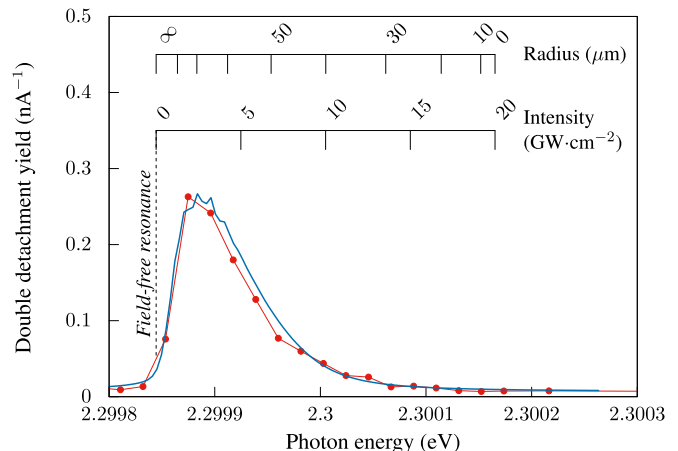


FIG. 5. Details of the $1s9d$ peak in the double detachment spectrum. Full circles: experiment, full line: simulation. Data is for linear polarization and 6 mJ laser pulses. The vertical dotted line indicates the position of the field-free $1s2s$ - $1s9d$ two-photon resonance. For larger photon energies, the $1s2s$ energy is Stark shifted and resonance condition is met for different laser intensities, as indicated by the intensity scale. A given intensity corresponds to a particular radius with respect to the center of the laser profile, as indicated by the radius scale. This radius defines an effective interaction cylinder, within which production of He^+ can occur.

photon. In the present wavelength range, double photodetachment therefore occurs by photodetachment and (2+1) REMPI of $\text{He}(1s2s\ ^3S)$. Ionization from higher Rydberg levels, with n up to 115, has been studied by Wall *et al.* [40] using a two-photon laser excitation and static field ionization scheme. In the low photon energy range, a continuous, slowly rising background is observed. It can be attributed to the onset of the (1+1) REMPI of the $1s2p$ state through a one-photon resonance with the

526 1s3d state, located at $\lambda = 587.7$ nm (2.110 eV). Although
 527 we are still far detuned from this resonance, the contribu-
 528 tion of this two-photon process to the double detachment
 529 yield is non-negligible compared to the three-photon pro-
 530 cess examined here.

531 The detailed profile of the peaks in the double detach-
 532 ment spectrum, for example that corresponding to the
 533 1s2s-1s9d resonance shown in Fig. 5, provides additional
 534 information on the ionization dynamics. Note that in
 535 this case the simulation was performed for a 68 μm laser
 536 waist in order to match the width of the experimental
 537 peak. No vertical scaling was applied to the simulated
 538 data. The size of the waist has not been measured for
 539 the present wavelength range and deviations from the 54
 540 μm waist measured for the range from 685 nm to 730 nm
 541 are considered possible. The width of the peak is much
 542 larger than the laser bandwidth of 0.05 cm^{-1} ($6.2\ \mu\text{eV}$),
 543 and it is asymmetrical, with a pronounced spread to-
 544 wards higher photon energies. Processes leading to this
 545 type of profile are threefold, and have been partly dis-
 546 cussed in paper P1 and by other authors [40]. We first
 547 note that the 1s2s state is shifted down in energy for in-
 548 creasing laser intensities by the AC Stark shift, while the
 549 Rydberg series remain essentially unperturbed. There-
 550 fore, even if the laser is blue-detuned from the 1s2s-1s9d
 551 resonance, the increasing intensity experienced by the he-
 552 lium atom moving through the laser focus will *dynamically*
 553 bring the 1s2s state into resonance with the 1s9d
 554 state, where population transfer occurs. As the laser is
 555 further blue-detuned, the exact resonance condition
 556 is met at increasing intensities, until the value required
 557 exceeds the laser peak intensity. Assuming a Gaussian
 558 laser profile, the intensity at which resonance occurs cor-
 559 responds to a specific radius with respect to the center of
 560 the profile, and thus defines a certain interaction cylinder,
 561 within which production of He^+ can occur. The volume
 562 of this cylinder shrinks as detuning becomes larger, con-
 563 sequently decreasing the He^+ signal. Finally, close to a
 564 zero-field resonance, population transfer to the Rydberg
 565 state occurs early on as the atom crosses the laser focus.
 566 Therefore, the duration of the interaction between the
 567 Rydberg state and the laser field is long and the ioniza-
 568 tion probability high. Blue-detuning results in delayed
 569 population transfer, reduced interaction time and there-
 570 fore reduced ionization probability, also resulting in a
 571 drop in the He^+ yield.

573 Turning to circular polarization, Fig. 4(b) provides a
 574 particularly illustrative example of dipole selection rules.
 575 In the case of left circular polarization (σ^+), selection
 576 rules for a two-photon transition give $\Delta M = +2$. Ex-
 577 citation from the 1s2s state to a Rydberg 1sns state is
 578 therefore forbidden, and the 1sns peak in the He^+ spec-
 579 trum disappears. The same argument applies in the case
 580 of right circular polarization (σ^-), for which the selection
 581 rule is $\Delta M = -2$, hence leading to the same spectrum.

582 The evolution of double detachment as the polariza-
 583 tion is tuned from linear to left circular is shown in Fig. 6.
 584 Measurements were performed both for the 1s2s-1s9d and

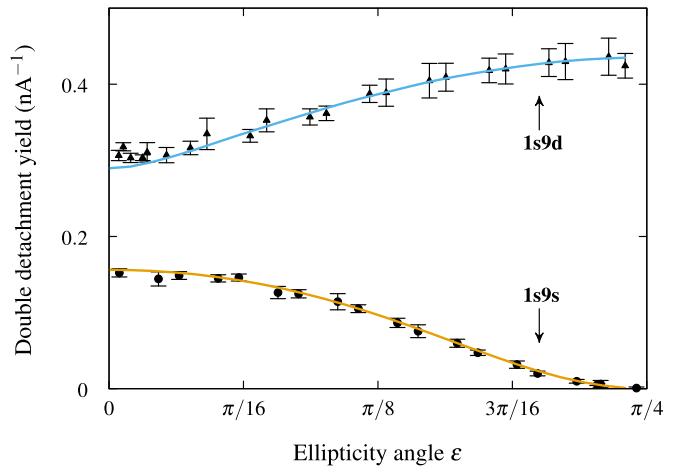


FIG. 6. Experimental and simulated double detachment yield as a function of the ellipticity angle. Triangles are experimental data for $\lambda = 539.08$ nm and correspond to resonance with the Rydberg 1s9d state. Circles are experimental data for $\lambda = 540.43$ nm and correspond to resonance with the Rydberg 1s9s state. Both full lines are the result of simulations for the same wavelengths, and have been scaled by 0.8 and 1.02 for the 1s9d and 1s9s states respectively.

585 1s2s-1s9s resonances, corresponding to photon energies of
 586 2.2999 eV and 2.2942 eV respectively, by stepwise rota-
 587 tion of the $\lambda/4$ plate while recording the corresponding
 588 He^+ signal. The effective Hamiltonian approach was used
 589 to simulate the experiment for the same photon energies,
 590 and the final results are scaled by 0.8 and 1.02 respec-
 591 tively in order to best fit the experimental values. We
 592 first note that the shape of the simulation curves follow
 593 the experimental data very well. The 1s9d peak ampli-
 594 tude increases as the polarization gets closer to circular,
 595 a fact that can be attributed to increasing coupling
 596 strength and ionization rate. For example, inspection of
 597 the value of the matrix element coupling the 1s2s state to
 598 the 1s9d state shows that, while the reduced matrix ele-
 599 ments are identical, geometrical factors arising from the
 600 polarization result in a coupling that is a factor 1.5 larger
 601 for circular polarization than for linear polarization. In
 602 sharp contrast, the amplitude of the 1s9s peak drops to
 603 zero as the polarization becomes circular, a direct result
 604 of the dipole selection rules.

2. Transient $\text{He}(1s2p\ ^3P^o)$ state

606 The double detachment of He^- for photon energies
 607 around 1.76 eV also exhibits resonance series, as can be
 608 seen in the experimental spectra shown in Fig 7. The
 609 spectrum for linear polarization has already been studied
 610 in paper P1, so we shall only recall the most important
 611 features before investigating the influence of the laser po-
 612 larization. In the present photon energy region, photode-
 613 tachment leaves helium in its 1s2s 3S and 1s2p $^3P^o$ states,
 614 and three-photon ionization of the latter is enhanced due

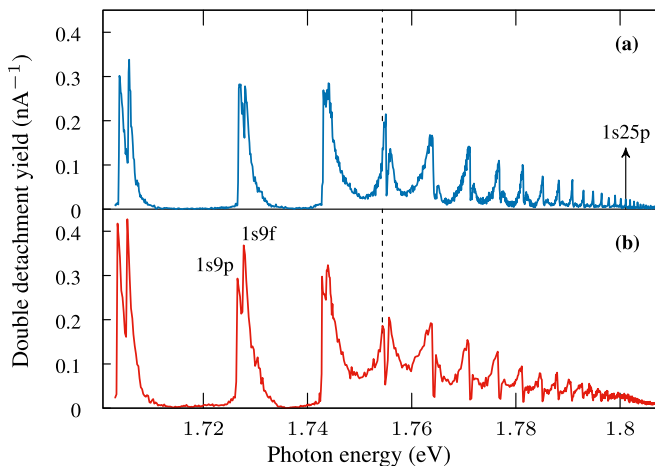


FIG. 7. Double detachment spectrum as a function of the photon energy. Top graph (a): linear polarization. Bottom graph (b): left circular polarization. The vertical dashed lines indicate the position of the $1s2p$ - $1s3s$ resonance. Resonances with Rydberg states are observed up to $n = 35$. The laser pulse energy is 6 mJ.

615 to two-photon resonances with Rydberg $1snp$ and $1snf$
 616 states. The shape of the spectrum is however very dif-
 617 ferent from that presented in Fig. 4 due to the presence
 618 of additional, one-photon resonances between the $1s2p$
 619 and $1s3s$ states and the $1s3s$ and $1snp$ states. Ioniza-
 620 tion proceeds either through $(1+1+1)$ REMPI *via* the
 621 $1s3s$ state and a Rydberg $1snp$ state, or through $(2+1)$
 622 REMPI preferentially *via* a $1snf$ Rydberg state. In linear
 623 polarization, the magnetic sublevel of $1s2p$ with $M_f = 0$
 624 ionizes through the $(1+1+1)$ scheme while those with
 625 $M_f = \pm 1$, which cannot couple to the $1s3s$ state, prefer-
 626 entially do so through the $(2+1)$ scheme.

627 In the detailed peak profiles presented in Fig. 8(a), the
 628 rightmost peak, corresponding to a $1snf$ resonance, exhib-
 629 its the same spread towards higher photon energies
 630 observed for the $\text{He}(1s2s\ ^3S)$ transient state, which can
 631 be attributed to the same dynamical processes. The left-
 632 most peak, corresponding to $1snp$ resonances, spreads in-
 633 stead towards lower photon energies, indicating that the
 634 $1s2p$ state is shifted up in energy. The spread however
 635 changes direction towards higher photon energies below
 636 the $1s2p$ - $1s3s$ resonance (see Fig. 7). This spreading and
 637 its reversal can be explained by the strong AC Stark shift
 638 of the $1s2p$ state due to the $1s3s$ state, which has opposite
 639 signs on either side of the resonance [18].

640 We next investigate the effect of polarization on the
 641 double detachment dynamics, and in particular on the
 642 respective contributions of the various magnetic sublevels
 643 of the $1s2p$ state. The detailed spectrum corresponding
 644 to resonances with $n = 13$ states is shown in Fig. 8, along
 645 with the simulated contributions from the $M_f = 0, \pm 1$
 646 magnetic sublevels. The most important difference be-
 647 tween linear and circular polarization is the change of
 648 shape of the $M_f = 0$ and $M_f = -1$ contributions to the

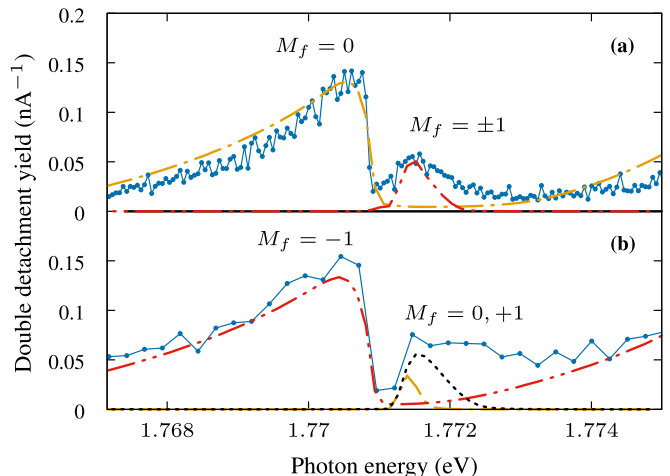


FIG. 8. Details of the double detachment spectrum around the $1s2p$ - $1s13p$ (left peak) and $1s2p$ - $1s13f$ (right peak) resonances. Top graph (a): linear polarization; bottom graph (b): left circular polarization. Full circles: experimental data, dash-dot-dot line: simulated $M_f = -1$ contribution, dash-dot line: simulated $M_f = 0$ contribution, dotted line: simulated $M_f = +1$ contribution. For linear polarization, $M_f = +1$ and $M_f = -1$ contributions are identical, therefore only twice the $M_f = -1$ contribution is shown. All simulated contributions are scaled by 0.45.

649 He^+ yield. For linear polarization, selection rules allow
 650 the $1s2p$ ($M_f=0$) state to couple to the $1s3s$ state, which
 651 itself couples to the $1s13p$ state, thus yielding a peak that
 652 is both broad, because of the strong AC Stark shift of the
 653 $1s2p$ state, and intense, due to the large enhancement of
 654 ionization by the $(1+1+1)$ channel. In the case of left
 655 circular polarization, coupling to the $1s3s$ state becomes
 656 allowed for the $M_f = -1$ magnetic sublevel, and the con-
 657 tributions of the various magnetic sublevels change ac-
 658 cordingly. Therefore, the attribution of the $1snp$ peaks
 659 to $M_f = 0$ and the $1snf$ peaks to $M_f = \pm 1$ for linear
 660 polarization changes to $M_f = -1$ and $M_f = 0, 1$ respec-
 661 tively for left circular polarization and to $M_f = 1$ and
 662 $M_f = -1, 0$ for right circular polarization. As a result,
 663 by carefully tuning the laser wavelength and polariza-
 664 tion, it is possible to address a specific magnetic sublevel
 665 of the initial state of the transient atom.

666 Apart from the changes in the different M_f contribu-
 667 tions, other differences in the shape of the peaks can be
 668 observed between the double detachment spectra for circular
 669 and linear polarization, in particular on the high
 670 photon energy side (see Figs. 7 and 8). These arise
 671 from two different effects and differ for the $1snp$ and $1snf$
 672 peaks. Let us first consider the $1snp$ peaks. Because of
 673 changes in the geometrical factors, the non-resonant AC
 674 Stark shift of the $1s2p$ ($M_f = -1$) sublevel for circular
 675 polarization is smaller than that of the $1s2p$ ($M_f = 0$)
 676 sublevel for linear polarization. Hence, since Rydberg
 677 series are unperturbed and the downward shift of the
 678 $1s2p$ energy is smaller, the peaks will spread less towards

679 higher photon energies. However, above the 1s2p-1s3s
 680 resonance, the 1s2p state will be significantly shifted up-
 681 ward in energy due to its interaction with the 1s3s state.
 682 The spread of the 1snp peak is therefore the result of a
 683 competition between the non-resonant and resonant AC
 684 Stark shifts, so that a smaller non-resonant contribution
 685 leads to an increased upward shift, and therefore an in-
 686 creased spread towards lower photon energies. In Fig. 8,
 687 the intensity of the 1snp peak is essentially the same for
 688 linear and circular polarization. Although the ionization
 689 rate of the 1snp states is 16% higher for circular polariza-
 690 tion, this increase is compensated by the lower (19%)
 691 population of the $M_f = -1$ sublevel for circular polariza-
 692 tion compared to that of the $M_f = 0$ sublevel for linear
 693 polarization.

694 Let us now consider the 1snf peak. For linear polariza-
 695 tion, contributions from $M_f = -1$ and $M_f = +1$ are
 696 strictly equivalent. This is no longer true in the case of
 697 circular polarization, and the $M_f = +1$ sublevel gives
 698 the dominant contribution while that for $M_f = 0$ is
 699 very similar to those for $M_f = \pm 1$ in the case of linear
 700 polarization. Investigating changes in matrix elements
 701 due to modified geometrical factors shows that the AC
 702 Stark shift of the 1s2p ($M_f = 0$) sublevel for circular
 703 polarization is identical to that of the 1s2p ($M_f = \pm 1$)
 704 sublevels for linear polarization, while that of the 1s2p
 705 ($M_f = 1$) sublevel is twice larger. Matrix elements cou-
 706 pling the 1s2p state with $M_f = 1$ to Rydberg 1snf states
 707 are also significantly larger for circular polarization. Fi-
 708 nally, the $M_f = 1$ sublevel is slightly more populated by
 709 photodetachment in circular polarization. Such increases
 710 explain why the 1snf peak becomes larger and signifi-
 711 cantly broadens when switching from linear to circular
 712 polarization.

713 Discrepancies between experimental and simulated
 714 yields, as observed in Fig. 8, may be due to variations in
 715 the transmission of the He^+ ions to the detector, slightly
 716 imperfect circular polarization of the laser light, imper-
 717 fect modeling of the experimental conditions and inaccura-
 718 cies in the effective Hamiltonian matrix elements.

719 Finally, the evolution of the double detachment yield
 720 as a function of the light polarization is shown in Fig. 9.
 721 The experimental yield was measured for a photon energy
 722 of 1.767 eV, chosen to probe the minimum between
 723 the 1s2p-1s12f and 1s2p-1s13p resonances, where the in-
 724 fluence of the polarization is most prominent. Simula-
 725 tions were also performed at the minimum, which in the
 726 calculations is located at a slightly lower photon energy
 727 (1.766 eV). The double detachment signal comes mainly
 728 from the 1s2p-1s13p resonance, with the contributions
 729 of the various magnetic sublevels evolving from predom-
 730 inantly $M_f = 0$ to mostly $M_f = -1$. The onset of
 731 the contribution from $M_f = +1$ as the polarization be-
 732 comes more circular is reminiscent of the broadening and
 733 increase in magnitude of the 1s2p-1snf peaks discussed
 734 above, with $n = 12$ here.

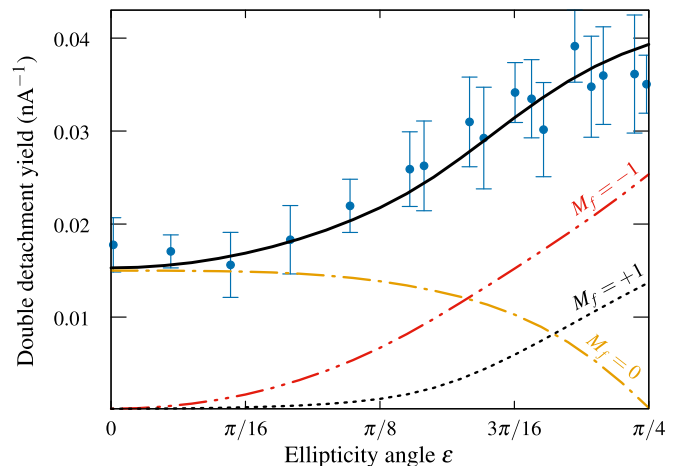


FIG. 9. Experimental and simulated double detachment yield as a function of the ellipticity angle, at the photon energy corresponding to the minimum between the 1s2p-1s12f and 1s2p-1s13p resonances. Full circles: experimental yield, full line: simulated yield, dash-dot-dot line: $M_f = -1$ contribution, dash-dot line: $M_f = 0$ contribution, dotted line: $M_f = +1$ contribution. The experimental yield is for a photon energy of 1.767 eV (701.72 nm) and the simulated one for 1.766 eV (702.05 nm). Simulated yields are scaled by 0.65 to match experimental values. The laser pulse energy is 6 mJ.

3. Sequential vs. non-sequential

735
 736 The above treatment considers photodetachment and
 737 REMPI as sequential events. Given the satisfactory
 738 agreement between simulated and measured ion yields,
 739 this appears reasonable. Detachment is indeed very effi-
 740 cient and occurs at low intensity, i.e., early in the pulse.
 741 The onset of REMPI requires much higher intensities and
 742 occurs later, when detachment is fully saturated. One
 743 possible exception is when the photon energy is tuned
 744 close to the 1s2p-1s3s resonance at 707 nm, since popu-
 745 lation transfer to the Rydberg states via the 1s3s state
 746 can take place very early in the pulse, at lower intensities
 747 where photodetachment is not yet saturated.

748 In order to establish the sequential nature of the dou-
 749 ble detachment process close the 1s2p-1s3s resonance,
 750 we have performed a two-color experiment where helium
 751 atoms are first prepared in the 1s2p state by photode-
 752 tachment by a CW laser tuned to $\lambda = 1005$ nm, and
 753 subsequently ionized downstream by the second, pulsed
 754 dye laser used previously. The two laser beams are spa-
 755 tially separated, and we select those He^+ ions that result
 756 from photodetachment by the first laser followed by mul-
 757 tiphoton ionization by the second.

758 The resulting double detachment spectrum is shown
 759 in Fig. 10 and compared with the one-laser spectrum,
 760 where detachment and ionization occur within the same
 761 laser pulse. Since the first laser in the two-color exper-
 762 iment is less efficient in producing helium atoms, the
 763 measured yield is smaller and was scaled in Fig. 10 in
 764 order to directly compare with the one-color spectrum.
 765

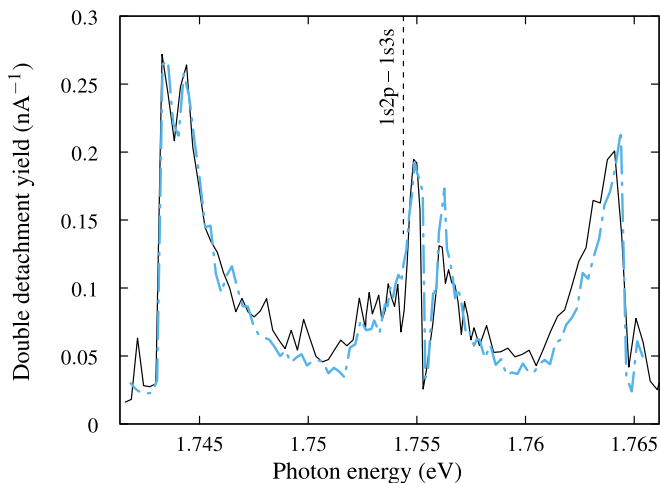


FIG. 10. Double detachment spectrum around the $1s2p$ - $1s3s$ resonance. Dot-dashed line: two-color, sequential measurement, multiplied by 35; full line: one-color measurement. The vertical dotted line indicates the exact position of the $1s2p$ - $1s3s$ resonance. The laser pulse energy is 6 mJ.

No significant differences can be seen, suggesting that no strong non-sequential processes occur. The experiment was run for linear polarization and we have also observed that, when the two laser polarizations are parallel or perpendicular, essentially the same spectra are obtained, to within experimental error bars.

The absence of any non-sequential process is not surprising considering the moderate laser intensities in our experiments (of the order of 10^{10} W/cm²). The dominant mechanism for non-sequential double ionization is the recollision of the first photoelectron with the residual atom or ion. The laser intensity required for this process can be estimated using the semi-classical recollision model [41, 42]. For wavelengths around 707 nm corresponding to the $1s2p$ - $1s3s$ resonance, intensities of over 8×10^{11} W/cm² would be necessary in order to eject the $11p$ electron. Coulomb focusing, which can greatly enhance the non-sequential double ionization rate of atoms and multiply charged ions [43], does not occur here since the recollision is with a neutral atom.

V. CONCLUSION

We have reported a joint experimental and theoretical investigation of the double detachment of He^- in moderately strong laser fields, for wavelengths ranging from 530 nm to 560 nm and from 685 nm to 730 nm, for various polarizations of the laser light. The experiment relies on counting He^+ ions, produced from a He^- beam by 6 mJ laser pulses, as a function of the wavelength and ellipticity angle. The theoretical work treats double detachment in two, sequential steps. The single detachment step is studied within an R -matrix approach by calculating branching ratios into the various final atomic

states and their magnetic sublevels for arbitrary elliptical polarization. Subsequent ionization of the neutral atom is studied using effective Hamiltonian models designed to account for all possible polarizations. They allow lightweight calculations which reproduce faithfully the experimental conditions.

The observed double detachment yield contains series of peaks arising from resonances between the initial state of the transient atom and Rydberg series. In the range from 530 nm to 560 nm, the $1s2s$ state produced by photodetachment is coupled, *via* a two-photon transition, to Rydberg $1sns$ and $1snd$ states. In this case, we showed that double detachment proceeds through single detachment and (2+1) REMPI of the neutral. In the range from 685 nm to 730 nm, the $1s2p$ state of the atom is resonantly coupled by one photon to the $1s3s$ state and by two photons to the $1snp$ and $1snf$ Rydberg series. Double detachment proceeds in this case through single detachment and both (1+1+1) and (2+1) REMPI of the atom.

The influence of the laser polarization is manifest in the $1s2s$ case, where $1sns$ resonances disappear for circular polarization as a result of the dipole selection rules. Changes in the double detachment spectrum induced by different polarizations are further explained in terms of geometrical factors. In the $1s2p$ case, the magnetic quantum number M_f strongly influences double detachment and determines the ionization pathway in the neutral atom. Changing the polarization from linear to elliptical and circular substantially modifies the various M_f contributions, which could be computed with the theoretical model. Differences in the shape of the double detachment spectra are further explained by geometrical factors and the slight orientation of the atom produced by photodetachment. Finally, the sequential nature of double detachment was assessed by a two-laser experiment and no evidence of non-sequential processes was found.

The study of double detachment of He^- in more intense laser fields is certainly of great interest since a comparison with lower intensities, where multiphoton processes dominate, is now possible. The present work could help disentangle sequential and non-sequential processes. Moreover, the influence of the magnetic quantum number M in strong field double detachment is expected to be important [8, 9], and the present work provides a detailed understanding of this influence in the relatively low intensity region. Finally, photoelectron spectroscopy of the present process could be a perspective for future work since it would provide additional information in terms of double detachment channels and angular distributions.

ACKNOWLEDGMENTS

This work was supported by the Fonds de la Recherche Scientifique-FNRS through IISN Contract No. 4.4504.10. Computational resources have been provided by the supercomputing facilities of the Université catholique

853 de Louvain (CISM/UCL) and the Consortium des
 854 Équipements de Calcul Intensif en Fédération Wallonie
 855 Bruxelles (CÉCI) funded by the Fonds de la Recherche
 856 Scientifique de Belgique (F.R.S.-FNRS) under conven-
 857 tion 2.5020.11, as well as by the Institut de Physique de
 858 Rennes.

859 **Appendix: Reduced dipole matrix elements for the**
 860 **photodetachment of He⁻**

861 The reduced dipole matrix elements
 862 $(\alpha_f L_f \ell L || \mathbf{D} || \alpha_i L_i)$ required when evaluating Eq. (3)
 863 for the partial cross sections were extracted from a
 864 standard R -matrix calculation. Here, we give details of
 865 this calculation, together with some illustrative results
 866 to assess the reliability of the reduced dipole matrix
 867 elements thus obtained.

868 In the R -matrix approach, configuration space is di-
 869 vided into two regions by a sphere encompassing the
 870 charge density of all states of the residual atom included
 871 in the calculation. Within this sphere, the states of the
 872 $(N + 1)$ -electron system are represented by a discrete
 873 set of antisymmetrized basis functions built from linear
 874 combinations of the residual atomic states coupled with
 875 a set of continuum orbitals representing the ejected elec-
 876 tron, supplemented by a number of bound or short-range
 877 correlation configurations. The $(N + 1)$ -electron Hamil-
 878 tonian is diagonalized in this basis, and the resulting
 879 eigenvalues and eigenvectors are used to construct the
 880 inverse logarithmic derivative matrix or R -matrix on the
 881 boundary of the inner region. In the outer region, the
 882 ejected electron moves far from the target while the other
 883 electrons remain bound. Exchange between the ejected
 884 and bound electrons can then be neglected, so that the
 885 wavefunctions for the full system can be represented by
 886 a standard close-coupling expansion involving products
 887 of the residual atomic states and a set of unknown func-
 888 tions representing the ejected electron. These unknown
 889 functions satisfy an infinite set of coupled second-order
 890 differential equations, with the appropriate asymptotic
 891 boundary conditions determining if the solutions repre-
 892 sent a bound state of the initial anion or a continuum
 893 state of the atom plus ejected electron. The initial bound
 894 state and final continuum states are then determined by
 895 matching the solutions in the inner and outer regions
 896 at their common boundary. For the initial bound state,
 897 this matching can only be performed at discrete energies,
 898 which are found by an iterative search algorithm.

899 Since the initial He⁻ anion has a ⁴P^o symmetry, after
 900 photodetachment the residual helium atom can only be
 901 left in a triplet state. The present calculation includes the
 902 five lowest triplet states of helium, whose wave functions
 903 were obtained using the CIV3 atomic structure computer
 904 code [44]. This code is based on a configuration inter-
 905 action approach, in which the wavefunctions for a par-
 906 ticular symmetry $|LS\pi\rangle$ are expressed as antisymmetric
 907 linear combinations of products of one-electron orbitals.

TABLE I. Slater orbital parameters used to build the helium
 triplet state wavefunctions.

	C_{jnl}	I_{jnl}	ζ_{jnl}		C_{jnl}	I_{jnl}	ζ_{jnl}
1s	5.65685	1	2.00000	2p	0.25282	2	0.54467
2s	1.02331	1	1.57920	3p	0.14871	2	0.50810
	-0.33960	2	0.59932		-0.00928	3	0.31496
3s	0.51628	1	1.53349	$\bar{4}p$	5.69931	2	1.81486
	-0.18699	2	0.46220		-0.14792	3	0.88532
	0.02242	3	0.37501		0.00010	4	0.31256
$\bar{4}s$	3.72051	1	0.57067	$\bar{5}p$	7.08316	2	2.03268
	-23.34422	2	1.97582		-1.97318	3	0.90825
	7.95138	3	1.78719		0.75867	4	1.01816
	-1.16998	4	1.23540		-0.00003	5	0.35646
$\bar{5}s$	11.03473	1	1.17185	3d	0.00904	3	0.33361
	-24.98834	2	1.09440		$\bar{4}d$	1.20358	3
	15.71030	3	1.09465	-0.00025		4	0.36349
	-3.08663	4	0.98350	$\bar{4}f$		0.57024	4
	0.46320	5	1.03562				

908 In CIV3, the radial part of each orbital is written as a
 909 sum of Slater orbitals:

$$P_{nl}(r) = \sum_{j=1}^k C_{jnl} r^{I_{jnl}} \exp(-\zeta_{jnl} r). \quad (\text{A.1})$$

910 The coefficients C_{jnl} are uniquely determined by or-
 911 thonormality constraints if $k = n - \ell$, while the in-
 912 dices I_{jnl} and the exponents ζ_{jnl} are variational param-
 913 eters chosen to minimize the energies of particular atomic
 914 states.

915 The values of the parameters used in the current study
 916 are given in table I. The 1s orbital is simply that for
 917 the hydrogenic He⁺ ion. The $n = 2, 3$ orbitals were all
 918 optimized on the associated $1sn\ell$ state of helium. The
 919 pseudo-orbitals $\bar{4}s$ and $\bar{5}s$ were optimized on the $1s2s$ ³S
 920 state, $\bar{4}d$ and $\bar{4}f$ on the $1s2p$ ³P^o state. The $\bar{4}p$ and
 921 $\bar{5}p$ pseudo-orbitals were optimized on a linear combina-
 922 tion of the $1s2p$ ³P^o and $1s3p$ ³P^o states as it was found
 923 that this gave the best energy separation between the two
 924 states.

925 The energies and excitation thresholds thus obtained
 926 are presented in table II, where they are compared with
 927 those of a more accurate calculation [35] and with the val-
 928 ues recommended by the National Institute of Standards
 929 and Technology (NIST). Oscillator strengths and transi-
 930 tion probabilities are compared with the NIST values in
 931 table III.

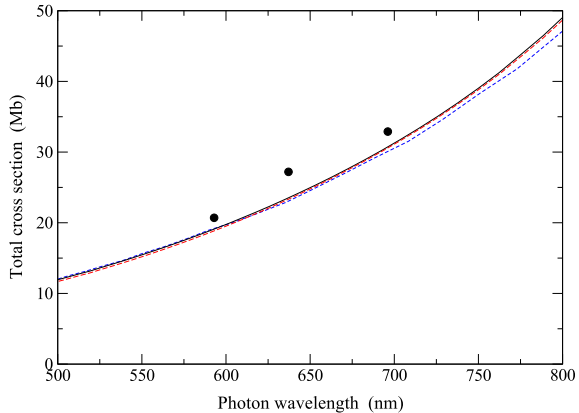


FIG. 11. Total cross section for the photodetachment of He^- as a function of the photon wavelength. Full line: R -matrix calculation using the length form of the dipole matrix elements; dashed line: R -matrix calculation using the velocity form of the dipole matrix elements; broken line: reference [11]; circles: experimental results from reference [13].

932 In the R -matrix calculation, the inner region extends
 933 out to $40 a_0$, and 30 continuum orbitals per angular mo-
 934 mentum ℓ are used to represent the ejected electron. The
 935 $(N + 1)$ -electron Hamiltonian in the inner region is diag-
 936 onalized for the initial $^4\text{P}^\circ$ symmetry and the three final
 937 symmetries ^4S , ^4P , ^4D allowed by the dipole selection
 938 rules. In the outer region, imposing decaying boundary
 939 conditions on the solutions of the coupled second-order
 940 differential equations in the $^4\text{P}^\circ$ symmetry yields an elec-
 941 tron affinity of about 75.5 meV for the initial He^- state.
 942 This compares favourably with the value of 77.518 meV
 943 obtained by a more extensive calculation [39], the ex-
 944 perimental value of 77.516 meV [39], and is slightly bet-
 945 ter than that of an earlier R -matrix calculation [11], in
 946 which the computed electron affinity was then slightly
 947 adjusted to agree with the accurate value. While such
 948 small differences may be important close to threshold,
 949 they have little effect on the overall cross sections in the
 950 range of photon wavelengths (500-800 nm) considered in
 951 this study, and we do not perform such an adjustment
 952 here. As shown in figure 11, presenting the total cross
 953 section for photodetachment of He^- , the agreement with
 954 the earlier work is very good [11].

TABLE II. Energies and excitation thresholds for the five lowest triplet states of helium. The theoretical values are compared with the accurate, non-relativistic energies taken from chapter 11 of [35] and the thresholds recommended by the National Institute of Standards and Technology (NIST) [34].

		Present (au)	Accurate (au)	Present (eV)	NIST (eV)
1s2s	2^3S	-2.17513	-2.17523	0.0	0.0
1s2p	2^3P^o	-2.13294	-2.13316	1.14805	1.14449
1s3s	3^3S	-2.06866	-2.06869	2.89720	2.89885
1s3p	3^3P^o	-2.05798	-2.05808	3.18754	3.18746
1s3d	3^3D	-2.05562	-2.05564	3.25203	3.25404

TABLE III. Oscillator strengths f and rates A in length (L) and velocity (V) forms for dipole allowed transitions involving the five lowest triplet states of helium, compared with the values recommended by NIST [34]. The figures in parentheses are the powers of ten by which the preceding number must be multiplied.

Transitions		f		A (sec $^{-1}$)	
		Present	NIST	Present	NIST
1s2s 3S - 1s2p $^3P^o$	L	0.5421	0.5394	0.1033 (8)	0.1022 (8)
	V	0.5320		0.1014 (8)	
1s2s 3S - 1s3p $^3P^o$	L	0.5744 (-1)	0.6448 (-1)	0.8442 (7)	0.9475 (7)
	V	0.6378 (-1)		0.9373 (7)	
1s2p $^3P^o$ - 1s3s 3S	L	0.7019 (-1)	0.6951 (-1)	0.2795 (8)	0.2785 (8)
	V	0.6786 (-1)		0.2703 (8)	
1s2p $^3P^o$ - 1s3d 3D	L	0.6161	0.6102	0.7100 (8)	0.7070 (8)
	V	0.6085		0.7012 (8)	
1s3s 3S - 1s3p $^3P^o$	L	0.9126	0.8914	0.1114 (7)	0.1074 (7)
	V	0.8693		0.1061 (7)	
1s3p $^3P^o$ - 1s3d 3D	L	0.1095	0.1120	0.1179 (5)	0.1292 (5)
	V	0.1055		0.1136 (5)	

- [1] T. Andersen, Phys. Rep. **394**, 157 (2004).
- [2] H. Stapelfeldt and H. K. Haugen, Phys. Rev. Lett. **69**, 2638 (1992).
- [3] H. Stapelfeldt, P. Kristensen, U. Ljungblad, T. Andersen, and H. K. Haugen, Phys. Rev. A **50**, 1618 (1994).
- [4] V. V. Petrunin, J. D. Voldstad, P. Balling, P. Kristensen, T. Andersen, and H. K. Haugen, Phys. Rev. Lett. **75**, 1911 (1995).
- [5] J. B. Greenwood, G. F. Collins, J. Pedregosa-Gutierrez, J. McKenna, A. Murphy, and J. T. Costello, J. Phys. B At. Mol. Opt. Phys. **36**, L235 (2003).
- [6] J. Pedregosa-Gutierrez, P. A. Orr, J. B. Greenwood, A. Murphy, J. T. Costello, K. Zrost, T. Ergler, R. Moshhammer, and J. Ullrich, Phys. Rev. Lett. **93**, 223001 (2004).
- [7] B. Bergues, Y. Ni, H. Helm, and I. Y. Kiyani, Phys. Rev. Lett. **95**, 263002 (2005).
- [8] H. W. van der Hart, Phys. Rev. A **74**, 053406 (2006).
- [9] B. Bergues and I. Y. Kiyani, Phys. Rev. Lett. **100**, 143004 (2008).
- [10] A. Gazibegović-Busuladžić, D. B. Milošević, W. Becker, B. Bergues, H. Hultgren, and I. Y. Kiyani, Phys. Rev. Lett. **104**, 103004 (2010).
- [11] C. A. Ramsbottom and K. L. Bell, J. Phys. B At. Mol. Opt. Phys. **32**, 1315 (1999).
- [12] J. Xi and C. Froese Fischer, Phys. Rev. A **53**, 3169 (1996).
- [13] D. J. Pegg, J. S. Thompson, J. Dellwo, R. N. Compton, and G. D. Alton, Phys. Rev. Lett. **64**, 278 (1990).
- [14] F. Dunning and R. Stebbings, Phys. Rev. Lett. **32**, 1286 (1974).
- [15] L. A. Lompré, G. Mainfray, B. Mathieu, G. Watel, M. Aymar, and M. Crance, J. Phys. B At. Mol. Phys. **13**, 1799 (1980).
- [16] H. Haberland, M. Oswald, and J. T. Broad, J. Phys. B At. Mol. Phys. **20**, 3367 (1987).
- [17] H. Haberland and M. Oswald, J. Phys. B At. Mol. Opt. Phys. **21**, 1183 (1988).
- [18] M. Génévriez, X. Urbain, M. Brouri, A. P. O'Connor, K. M. Dunseath, and M. Terao-Dunseath, Phys. Rev. A **89**, 053430 (2014).
- [19] P. Reinherd, A. Orbán, J. Werner, S. Rosén, R. D. Thomas, I. Kashperka, H. A. B. Johansson, D. Misra, L. Brännholm, M. Björkhage, H. Cederquist, and H. T. Schmidt, Phys. Rev. Lett. **103**, 213002 (2009).
- [20] C. W. Walter, J. A. Seifert, and J. R. Peterson, Phys. Rev. A **50**, 2257 (1994).
- [21] J. R. Peterson, Y. K. Bae, and D. L. Huestis, Phys. Rev. Lett. **55**, 692 (1985).
- [22] P. A. Závodszky, L. Sarkadi, L. Víkor, and J. Pálincás, Phys. Rev. A **50**, R899 (1994).
- [23] M. Bylicki, J. Phys. B At. Mol. Opt. Phys. **30**, 189 (1997).
- [24] D.-S. Kim, H.-L. Zhou, and S. T. Manson, Phys. Rev. A **55**, 414 (1997).
- [25] C. A. Nicolaides and T. Mercouris, J. Phys. B At. Mol. Opt. Phys. **29**, 1151 (1996).
- [26] P. G. Burke, *R-Matrix Theory of Atomic Collisions*, Springer Series on Atomic, Optical, and Plasma Physics, Vol. 61 (Springer, Berlin, Heidelberg, 2011).
- [27] A. M. Tumaikin and V. I. Yudin, Sov. Phys. JETP **71**, 43 (1990).
- [28] A. V. Taichenachev, A. M. Tumaikin, V. I. Yudin, and G. Nienhuis, Phys. Rev. A **69**, 033410 (2004).
- [29] A. R. Edmonds, *Angular Momentum in Quantum Mechanics* (Princeton University Press, London, 1996).
- [30] “UK APAP (Atomic Processes for Astrophysical Plasmas network,” <http://www.apap-network.org/>.
- [31] J. P. Killingbeck and G. Jolicard, J. Phys. A. Math. Gen. **36**, R105 (2003).
- [32] G. Jolicard and J. P. Killingbeck, J. Phys. A. Math. Gen. **36**, R411 (2003).
- [33] P. Durand, Phys. Rev. A **28**, 3184 (1983).
- [34] A. Kramida, Y. Ralchenko, J. Reader, and NIST ASD Team, “NIST Atomic Spectra Database,” <http://www.nist.gov/pml/data/asd.cfm> (2016).
- [35] G. Drake, ed., *Springer Handbook of Atomic, Molecular, and Optical Physics*, Vol. 1 (Springer New York, New York, NY, 2006).
- [36] B. W. Shore, *The Theory of Coherent Atomic Excitation, Vol. 2, Multilevel Atoms and Incoherence* (Wiley, New York, 1990).
- [37] H. C. Baker, Phys. Rev. A **30**, 773 (1984).
- [38] R. B. Sidje, ACM Trans. Math. Softw. **24**, 130 (1998).
- [39] P. Kristensen, U. V. Pedersen, V. V. Petrunin, T. Andersen, and K. T. Chung, Phys. Rev. A **55**, 978 (1997).
- [40] T. E. Wall, D. B. Cassidy, and S. D. Hogan, Phys. Rev. A **90**, 053430 (2014).
- [41] P. B. Corkum, Phys. Rev. Lett. **71**, 1994 (1993).
- [42] K. C. Kulander, K. J. Schafer, and J. L. Krause, “Superintense laser-atom physics,” (New York: Plenum Press, 1993).
- [43] T. Brabec, M. Y. Ivanov, and P. B. Corkum, Phys. Rev. A **54**, R2551 (1996).
- [44] A. Hibbert, Comput. Phys. Commun. **9**, 141 (1975).